Observed and GCM-Simulated Westward-Propagating, Planetary-Scale Fluctuations with Approximately Three-Week Periods

NGAR-CHEUNG LAU AND MARY JO NATH

Geophysical Fluid Dynamics Laboratory/NOAA, Princeton University, Princeton, New Jersey

ABSTRACT

The structural characteristics and vorticity dynamics of westward-traveling patterns (WTP) in the troposphere are examined using the National Centers for Environmental Prediction–National Center for Atmospheric Research (NCEP–NCAR) reanalyses based on observations for the 1973–95 period, as well as the output from a 100-yr integration of a general circulation model (GCM) with a rhomboidal truncation at 30 wavenumbers and 14 vertical levels. An identical set of diagnostic tools, including progressive/retrogressive variance analysis, cross-spectra, and complex empirical orthogonal functions (EOFs), are applied to the reanalysis and GCM datasets for 300-mb height. These diagnoses all indicate that the WTP are most prominent during the cold season in the high-latitude zone extending westward from northwestern Canada to northeastern Siberia, with a typical period of ~22 days. Outstanding episodes are identified on the basis of the temporal coefficients of the leading complex EOF. Composite charts of the anomalous 300-mb height, sea level pressure, and 850-mb temperature fields at various phases of these events are constructed. The typical circulation changes accompanying the passage of the WTP are similar to those associated with well-known regional weather phenomena such as amplified pressure ridges over Alaska, cold air outbreaks over western North America and east Asia, and heavy snowfall over the Pacific Northwest. The occurrence of the WTP over the North Pacific is also characterized by notable changes in the spatial distribution and intensity of synoptic scale activity.

The contributions of relative vorticity advection, planetary vorticity advection (the "β effect"), and horizontal divergence to the vorticity tendency in various phases of the composite wave at 300, 500, and 850 mb are investigated. In the mid- and upper troposphere, the vorticity dynamics of the WTP is similar to that of free external Rossby waves, with the β effect (which leads to westward propagation) being the dominant term, whereas the eastward advection of relative vorticity is less important due to the weak mean zonal flow in the Alaska–Siberia sector.

Most of the essential characteristics of the observed WTP deduced from the NCEP–NCAR reanalyses are well reproduced by the GCM. The realism with which this phenomenon can be simulated in a model environment offers considerable promise for using the GCM as a tool for studying the impact of WTP on intraseasonal atmospheric variability in extended model experiments, and for assessing the dependence of the locality and activity level of the WTP on various states of the ambient circulation.

1. Introduction

The propagational and structural characteristics of large-scale atmospheric waves have long been a subject of considerable interest to the meteorological community. These phenomena contribute significantly to atmospheric variability on a broad range of timescales and are hence crucial for a comprehensive understanding of the general circulation. Our improved knowledge of the dynamical processes associated with some of these long-lived and coherent wave features may also find applications in extended-range weather forecasting.

The basic groundwork for analyzing the behavior of

planetary-scale waves was laid in the landmark paper by Rossby et al. (1939). By invoking the conservation of absolute vorticity, it was shown that the "Rossby waves" travel westward relative to the mean zonal current. Rossby's work was subsequently extended by Haurwitz (1940a,b) to incorporate the effects of the earth's spherical geometry. It was recognized that the wave motions considered by Rossby and Haurwitz are special cases of free oscillations of the terrestrial atmosphere. Solutions to the horizontal structure equation of these free waves have been sought by Hough (1898) using spherical harmonics. Such solutions were later referred to as "Hough functions." A detailed historical account of the advances in our theoretical understanding of the Rossby waves can be found in the excellent review articles by Platzman (1968), Madden (1979), and Salby (1984).

When synoptic observations with worldwide cover-

Corresponding author address: Dr. Ngar-Cheung Lau, Geophysical Fluid Dynamics Laboratory, P.O. Box 308, Princeton University, Princeton, NJ 08542.
E-mail: gl@gfdl.gov

age became available in the postwar years, attempts were made by a multitude of investigators to search for the free Rossby wave modes in the real atmosphere. Most of the earlier studies were aimed at matching the observational data with the eigensolutions of the governing equations for the atmospheric modes. The data fields were either decomposed into zonal harmonics (e.g., Deland 1964; Arai 1970; Madden 1978; Madden and Speth 1989, among others) or spherical harmonics (e.g., Deland 1965; Eliasen and Machenhauer 1965; Ahlquist 1982; Lindzen et al. 1984, among others), so that the results could readily be compared with theory. Implicit in this analysis approach is the a priori assumption that the prevalent modes of atmospheric variability have strong spatial projections on sinusoidal waves around latitude circles, with specific nodal structures in the meridional direction. A summary of the earlier empirical studies using this paradigm is given in Table 4 of Madden (1979). The behavior of observed perturbations with zonal wavenumbers 1 and 2 corresponds well to that of external Rossby waves, with westward propagation, almost no vertical phase tilt in the troposphere, and amplitude increasing with height. The myriad observational studies have cited a wide range of periods (~3–40 days) for these waves. Of particular note are the 5-day wave [as identified by Madden and Julian (1972) based on cross-spectra between pressure fluctuations at individual stations], which bears some resemblance to the Hough function with zonal index $m = 1$ and meridional index $n = 2$, and the 16-day wave (Madden 1978), which may correspond to the Hough mode with $m = 1$ and $n = 4$. The typical amplitudes of the 5- and 16-day waves in the troposphere are 5–7 and 50–120 m in geopotential height, respectively. Lejenäs and Madden (1992) further noted that a considerable fraction of observed blocking episodes are coincident with westward-traveling waves with $m = 1$ and 2.

More recently, an alternative approach was adopted by Branstator (1987) and Kushnir (1987) to examine recurrent westward-traveling patterns (hereafter abbreviated as WTP) in the extratropics. Instead of expressing the data fields in terms of predetermined basis functions such as spherical harmonics or zonal Fourier series, these studies made use of empirical orthogonal functions (EOFs). In applying the latter analysis tool, the basis functions were constructed according to characteristic spatial structures of the data fields themselves. Branstator and Kushnir independently reported the existence of WTP in the 500-mb height field, with an averaged period of about three weeks and with particularly high amplitudes in the northern Canada–Alaska sector. It is unclear whether the WTP as identified by Branstator and Kushnir are associated with a particular Hough mode as predicted by the theory for free global-scale atmospheric oscillations.

The localization of the WTP in certain geographical regions suggests that the zonally asymmetric nature of the background circulation is an important consideration in understanding this phenomenon. In particular, the behavior of the WTP could be strongly influenced by the configuration of the stationary wave field and the location of the jet streams, and by the occurrence of eddy–mean flow interactions in specific regions. Recently, the barotropic vorticity equation has been used by Anderson (1991), Branstator and Held (1995), and Huang and Robinson (1995) to study the instability characteristics of the WTP in the presence of basic states with more realistic zonal asymmetries. It was shown by these investigators that the wavy background flow is capable of producing barotropic retrograde modes with periods, spatial structure, and regional dependence that are comparable to those discerned from observations.

The observational and modeling results cited in the two preceding paragraphs encourage us to conduct further diagnostic studies on the WTP by accentuating the role of local dynamical processes. Our intention here is to complement the earlier works of Branstator (1987) and Kushnir (1987) by documenting in fuller detail the space–time properties and vorticity dynamics of the WTP in both observed and model atmospheres. This primary objective is to be achieved by diagnosing the quality controlled global reanalysis dataset produced recently by the National Centers for Environmental Prediction (NCEP) and National Center for Atmospheric Research (NCAR) for the 1973–95 period, and the output from a century-long general circulation model (GCM) integration. We shall assess the fidelity of this GCM in reproducing the essential characteristics of the WTP by subjecting the model data and NCEP–NCAR data to an identical set of analysis procedures and then comparing the results. The diagnostic techniques to be applied in this study include spectral decomposition of the progressive and retrogressive variances, cross-spectra, complex EOFs, composite charts, and budget analysis of the vorticity tendency equation. By presenting the findings based on both GCM and reanalysis data, it is possible to evaluate the applicability of the GCM as a tool for further studies of various facets of the WTP. The inclusion of the two independent data sources in the present analysis also serves to enhance the reliability and credibility of our findings, especially those based on observational and GCM evidence that are in mutual agreement.

2. Datasets

The observational database for this study consists of the daily global analyses of geopotential height, wind, and temperature at selected pressure levels for the 23-yr period from 1973 through 1995. This dataset is a product of the NCEP–NCAR Reanalysis Project (see Kalnay et al. 1996 for further details). The daily means were obtained by averaging the four 6-hourly analyses for individual days. The original data grids have a horizontal resolution of 2.5° × 2.5°. For comparison with

the GCM results, these analyses have been interpolated to the Gaussian grid corresponding to a rhomboidal truncation at 30 wavenumbers, with a resolution of 3.75° (longitude) $\times$ ~2.22° (latitude). We shall henceforth refer to this dataset for the observed atmosphere as the NCEP–NCAR data or the reanalysis data.

The model output examined here was generated by a 100-yr integration with a global spectral GCM developed and maintained by the Climate Dynamics Project of the Geophysical Fluid Dynamics Laboratory (GFDL). The output of this experiment was archived at daily intervals. Horizontal variations in the model atmosphere are represented by spherical harmonics with rhomboidal truncation at 30 wavenumbers. Vertical variations are described at 14 sigma levels. In the course of the experiment, the prescribed sea surface temperature variations at the lower boundary evolve through 100 identical annual cycles; that is, no interannual variability in the oceanic conditions is introduced in this simulation. Realistic ocean–continent contrast and orography are incorporated in the GCM. The physical processes being treated by the model include seasonally varying insolation, radiative transfer, cloud formation, precipitation, ground hydrology, snow and ice cover, and gravity wave drag. Further details of the model formulation have been described by Broccoli and Manabe (1992). A comprehensive documentation of the climatological statistics of this GCM has been compiled by Alexander and Scott (1995). We shall henceforth refer to the dataset generated by this model as the GCM data.

For both NCEP–NCAR and GCM data, the mean climatological seasonal cycle has been obtained by first averaging the data for a given calendar day over all the available years, and then performing a 31-day running mean of the averages. On several occasions in this study, this mean seasonal cycle has been removed from the daily data for individual years to obtain anomalies.

Some of our computations also entail the application of a Lanczos filter (Duchon 1979) to the daily data. This filter retains fluctuations with periods between 10 and 45 days, and the filter weights have been computed for a maximum lag of 100 days. All time series that are subjected to this filtering procedure will henceforth be referred to as Lanczos-filtered data.

Throughout this study, the cold season is defined as the five-month periods of November–March for the Northern Hemisphere and May–September for the Southern Hemisphere. The warm season for the Northern Hemisphere is defined as the period of May–September.

3. Time-averaged circulation and its variability

We first describe some basic climatological statistics of the observed and simulated atmospheres. In Fig. 1 are shown the distributions during the cold season of the long-term averaged 300-mb zonal wind (Figs. 1a

and 1c), and root-mean-squares (rms) of Lanczos-filtered 300-mb height (Figs. 1b and 1d).

The GCM performs well in simulating the position and strength of the principal jet streams over eastern Asia, eastern North America, and North Africa (Figs. 1a and 1c). It is worth noting that, in both the GCM and NCEP–NCAR patterns, the zonal wind speed decreases rapidly poleward of the jet core over the western North Pacific and reaches near-zero values over northeastern Siberia. In general, some of the lowest zonal wind speeds are found in the subpolar zone extending westward from Alaska to northern Russia.

The maxima in Figs. 1b and 1d correspond to those regions with enhanced amplitude or frequency of occurrence of geopotential height fluctuations with periods of 10–45 days. Both GCM and NCEP–NCAR results indicate two regions of activity, one of which is centered near the Gulf of Alaska and protrudes northwestward to the Bering Sea and northern coast of Russia, and the other situated over the eastern North Atlantic and northern Europe. The rms amplitudes of the model-simulated perturbations are ~80% of the observed values.

4. Progressive/retrogressive variance analysis

Following the methodology described by Hayashi (1971), a spatial Fourier analysis has been performed on the daily 300-mb height data at each latitude, and a temporal Fourier analysis was then applied to the coefficients of the zonal harmonics. This procedure allows for the partitioning of the space–time variance into progressive (eastward traveling) and retrogressive (westward traveling) components associated with individual zonal wavenumbers and with individual temporal frequencies. For a given latitude, we denote the variance associated with progressive and retrogressive fluctuations for a specific zonal wavenumber m and a specific frequency f as $\text{Var}_p(m, f)$ and $\text{Var}_r(m, f)$, respectively. We also denote the sum of the variances associated with progressive and retrogressive components for all zonal wavenumbers at the same frequency f as $\text{Sum}(f)$, so that $\text{Sum}(f) = \Sigma_m [\text{Var}_p(m, f) + \text{Var}_r(m, f)]$.

At each latitude, the ratios $\text{Var}_p(m, f)/\text{Sum}(f)$ and $\text{Var}_r(m, f)/\text{Sum}(f)$ have been computed to assess the contributions of progressive and retrogressive disturbances at various zonal scales to the total variability at a specific timescale. The sums of these variance ratios for the first three zonal wavenumbers, that is, $\Sigma_{m=1}^{3} \text{Var}_p(m, f)/\text{Sum}(f)$ and $\Sigma_{m=1}^{3} \text{Var}_r(m, f)/\text{Sum}(f)$, are shown in Fig. 2 as a function of frequency and latitude for (a) GCM simulation and (b) NCEP–NCAR reanalyses in the November–March season.

Within the 60°–80°N latitude zone, retrograde disturbances with zonal wavenumbers 1–3 and with periods of ~20–40 days account for more than half of the variance at individual frequencies. The variance ratios for progressive waves at the same latitudes and frequency bands are notably lower, with typical values of ~25%.

GCM U **Reanalysis**
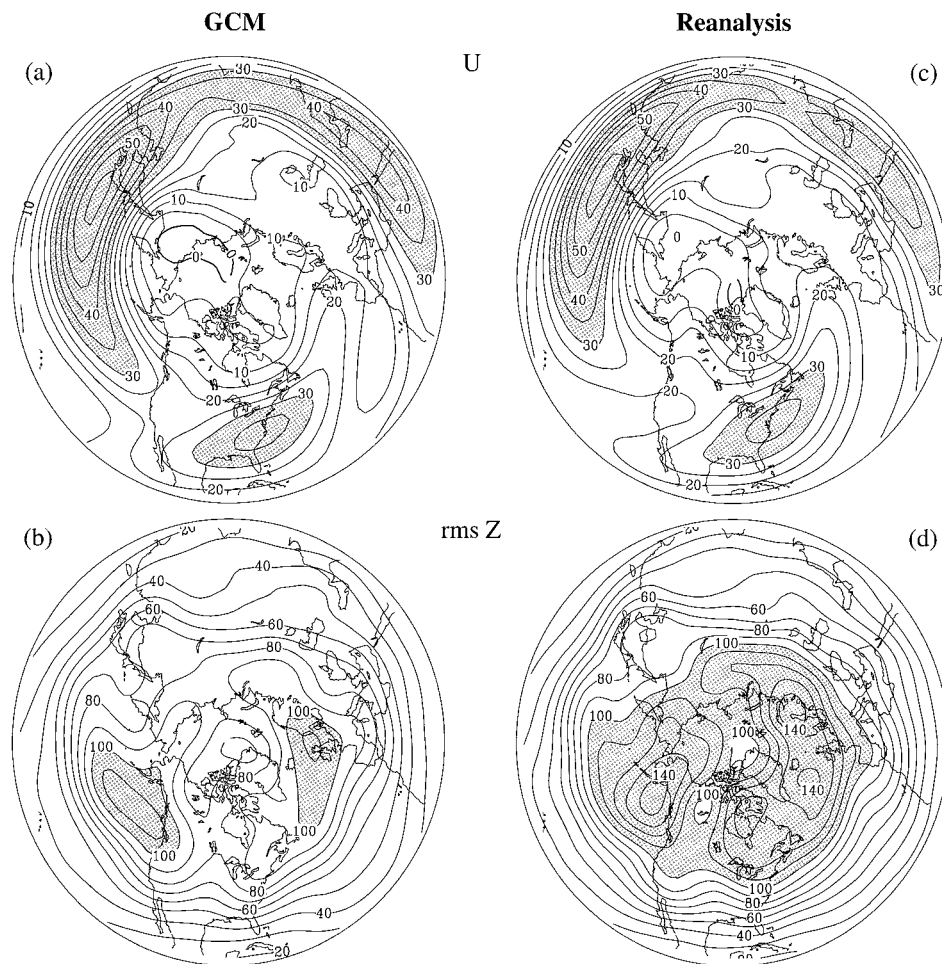
(a) (c)

(b) rms Z (d)

FIG. 1. Distributions of the GCM (left panels) and NCEP–NCAR (right panels) climatologies of 300-mb zonal wind [(a) and (c); contour interval: 5 m s^{-1}], and root-mean-squares of Lanczos-filtered 300-mb height [(b) and (d); contour interval: 10 m], for the cold season (November–March).

The other latitude zone where the retrogressive variance at 20–40-day timescales exceeds the corresponding progressive variance by a considerable margin is located near 75°S. Immediately equatorward of the latter zone, at about 60°S, is a region characterized by active eastward traveling waves. Also discernible from Fig. 2 are retrograde fluctuations with ~15–30-day periods in the subtropical zones at ~15°N and 15°S. Broad agreement exists between the GCM and NCEP–NCAR results, both with regard to the latitudinal distribution of the variance ratio and the partitioning of the variance into eastward- and westward-traveling components.

The contributions to the progressive and retrogressive variances by each of the first three zonal wavenumbers m are indicated in Table 1, which shows the variance ratio for individual m. Each variance ratio has been averaged over the 59°–79°N zone and the 15–38-day frequency band. The ratios for $m > 3$ (not shown) are smaller than those displayed in this table. For both the GCM and NCEP–NCAR data, the highest retrogressive

variance in the frequency band considered here is associated with wavenumber 1. Fluctuations with $m = 2$ also make a substantial contribution, whereas the variance ratio for $m = 3$ is much smaller. On the other hand, each of the first three zonal wavenumbers has similar contributions to the progressive variance.

The quantity displayed in Fig. 2 is a fraction of the total variance for a given frequency and latitude. This ratio serves to highlight those latitude and frequency bands in which the retrograde disturbances account for a large portion of the variance. However, the results in Fig. 2 are not suited for comparing the spectral power in different latitudes and the levels of variability in simulated and observed atmospheres. These comparisons can be made by inspecting charts of the actual variances at various time scales, such as those presented in Figs. 1b and 1d.

5. Cross-spectral analysis

A more detailed description of the spatio–temporal evolution accompanying the WTP can be obtained by
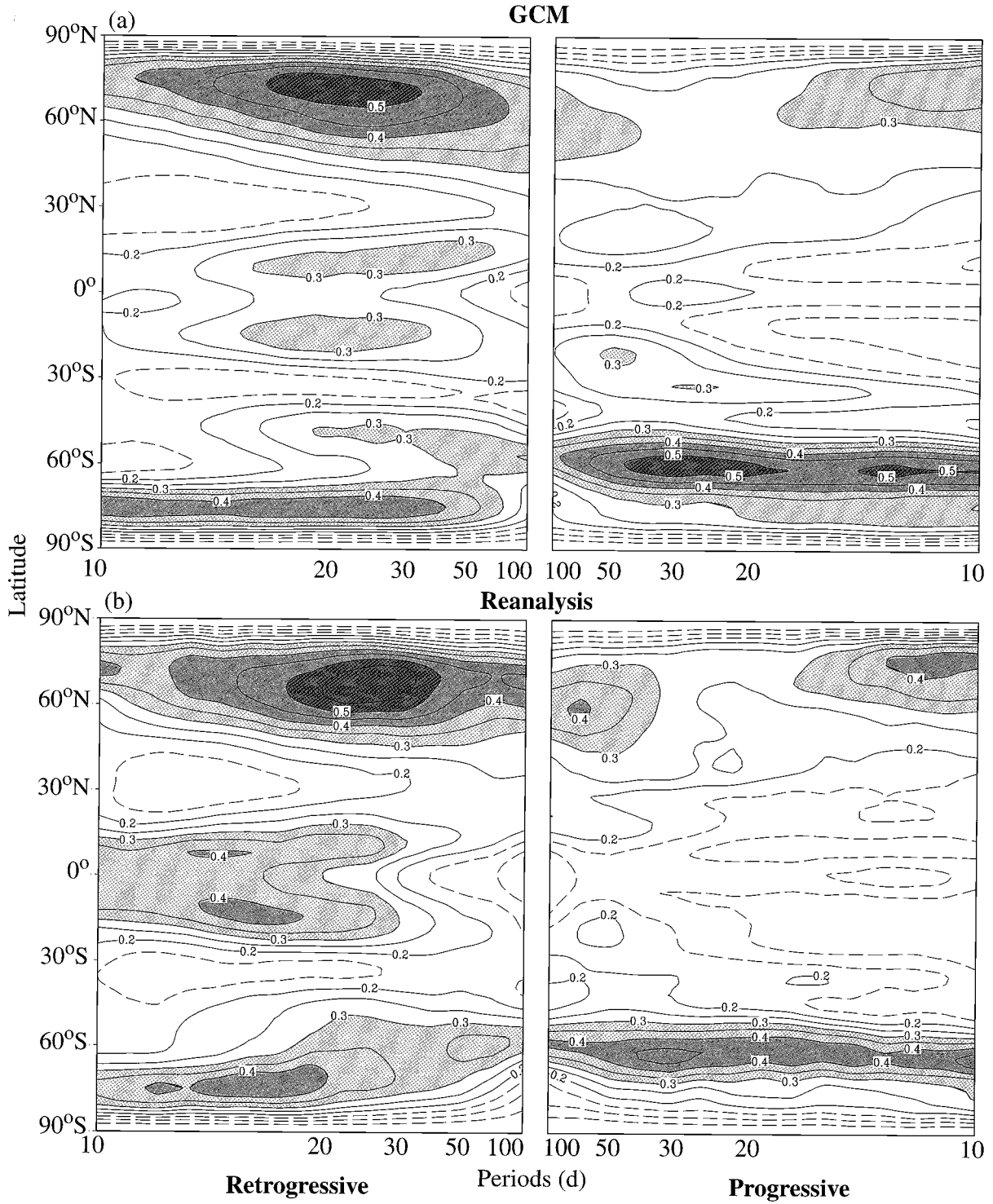
FIG. 2. Ratio of retrogressive (left panels) and progressive (right panels) variance in the first three zonal wavenumbers to the total variance for individual frequencies, plotted as a function of frequency and latitude. Contour interval: 0.05. Dashed contours indicate ratios of 0.15 and smaller. All computations are based on 300-mb height data from the GCM (upper panels) and NCEP–NCAR reanalyses (lower panels) for the November–March season.

TABLE 1. Fraction (in percent) of the variance of retrogressive and progressive disturbances associated with the first three individual zonal wavenumbers, as computed using 300-mb height data from the GCM and NCEP–NCAR reanalyses for the cold season. The results are obtained by averaging the variance fractions for the 59°–79°N zone, and for 15–38-day periods.

| Zonal wavenumber (m) | GCM | | Reanalysis | |
	Retrogressive variance	Progressive variance	Retrogressive variance	Progressive variance
1	25	10	28	10
2	16	10	17	10
3	6	8	6	8

mapping the coherence and phase of the fluctuations at individual grid points relative to the corresponding variations at a preselected reference site (RS). Time–longitude diagrams of the simulated 300-mb height anomalies in representative winters (not shown) indicate that the strongest retrograde activity occurs near the Arctic Circle from northern Canada through the Bering Sea to northern Russia, whereas the WTP are less prominent in the Atlantic and European sectors. We hence designated the grid point at 70°N, 180°E (which corresponds to the center of this active region) as the RS. For each selected grid point in the spatial domain of interest, a cross-spectral analysis has been performed on the pair of time series of daily 300-mb height at that grid point and at RS. Details of this analysis technique have been described by Lau and Nath (1987). All spectral quantities have been obtained using the lag-correlation method, with the number of lags being set to 20.

The horizontal distribution of the coherence and phase information obtained from the cross-spectral analysis is shown in Fig. 3 for (a) GCM and (b) NCEP–NCAR data for the northern cold season. The frequency band chosen for this display is centered at the 20-day period, with a bandwidth of 16–27 days. This choice of the frequency band has been made on the basis of the dominant timescale of retrograde disturbances, as inferred from the variance ratios displayed in Fig. 2 and from time–longitude plots of 300-mb height data (not shown). The phase difference between the fluctuations at RS and at a certain grid point is depicted using the orientation of an arrow plotted at the grid point. An arrow pointing due north represents an in-phase relationship between fluctuations at the arrow site and those at RS. The arrow rotates by 1° in the clockwise direction for each degree of phase lag of the variations at the arrow site relative to those at RS. Conversely, rotation in the counterclockwise direction indicates a phase lead relative to RS. For instance, an arrow pointing due east (west) corresponds to a 90° phase lag (lead) relative to RS, whereas a southward-pointing arrow implies an exact out-of-phase relationship.

The reliability of the phase estimation can be inferred from the significance level of the coherence squared for the pair of time series in question. Following Panofsky and Brier (1958), the threshold values of the coherence squared at various confidence levels have been determined from the number of degrees of freedom (DF),

which is in turn related to the length of the data record and the number of lags used in the cross-spectral analysis. The appropriate DF for the GCM and NCEP–NCAR datasets have been estimated using the method proposed by Julian (1975). Those regions with coherence squared exceeding the 80% and 99% significance levels are indicated in Fig. 3 by stippling of various densities.

The most salient feature in both the model and observed patterns in Fig. 3 is a zonally elongated band of coherent fluctuations situated poleward of 50°N and extending through much of northern Canada, Alaska, and eastern Siberia. The systematic clockwise rotation of the phase arrows in Fig. 3 from east to west confirms the prevalence in this zone of westward-propagating perturbations with 16–27-day periods. At ~60°N latitude, the arrows evolve through a half-cycle (8–14 days) between 120°W and 120°E, thus yielding a phase speed of 9°–15° of longitude per day. The zonal distance between arrows with a half-cycle phase difference also implies that the retrograde features have typical local wavelengths of ~240° of longitude. This estimate is consistent with the large contributions to retrogressive variance by wavenumbers 1 and 2 (see Table 1). Through much of the Pacific and Asian sectors, the high-latitude fluctuations at a given longitude are accompanied by subtropical fluctuations of the opposite polarity at the same longitude, with nodal lines appearing at ~40°N over the Pacific and at ~50°N over eastern Asia.

Comparison between the two panels in Fig. 3 reveals considerable similarities between the phase structure of the WTP appearing in the GCM and NCEP–NCAR reanalyses. The phase patterns shown here also resemble those presented by Branstator (1987, Fig. 13), Kushnir (1987, Fig. 3), Lanzante (1990, Fig. 4, for the mode labeled by that author as ''W1W'') based on observational data, and Anderson (1991, Figs. 1b and 5a) based on stability analysis of a barotropic model.

6. Complex EOF analysis

The phase characteristics of the prominent modes of variability could also be identified in an objective manner using complex EOF analysis. The procedure for conducting this analysis follows that described by Horel (1984). A Lanczos filter (see section 2) was first applied to the daily time series of the normalized 300-mb height
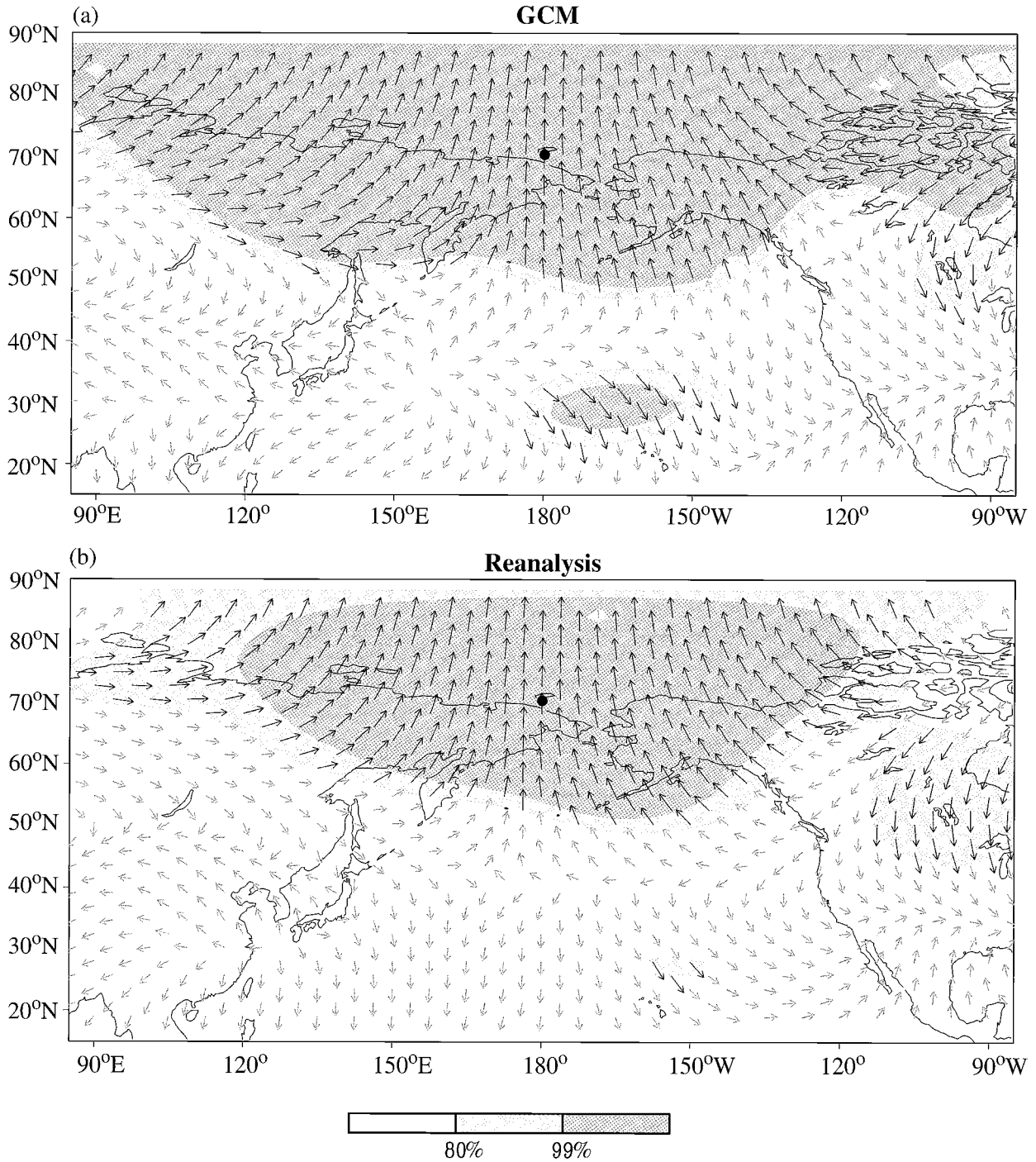
FIG. 3. Phase (arrows) between the 300-mb height fluctuations at individual grid points and the corresponding fluctuations at the reference site (RS, indicated by a large dot) at 70°N, 180°E, as deduced using cross-spectral analysis of (a) GCM and (b) NCEP–NCAR data for the cold season and for the frequency band centered at the 20-day period, with a 16–27-day bandwidth. Arrows pointing due north indicate an in-phase relationship between the local fluctuations and those at RS. Clockwise (counterclockwise) rotations of the arrows indicate phase lags (leads) of the local fluctuations relative to those at RS, at the rate of one degree per degree of phase difference. Regions with values of coherence squared exceeding various significance levels are indicated by stippling (see scale bar at bottom). Short and gray arrows are plotted at grid points with significance levels lower than 80%.
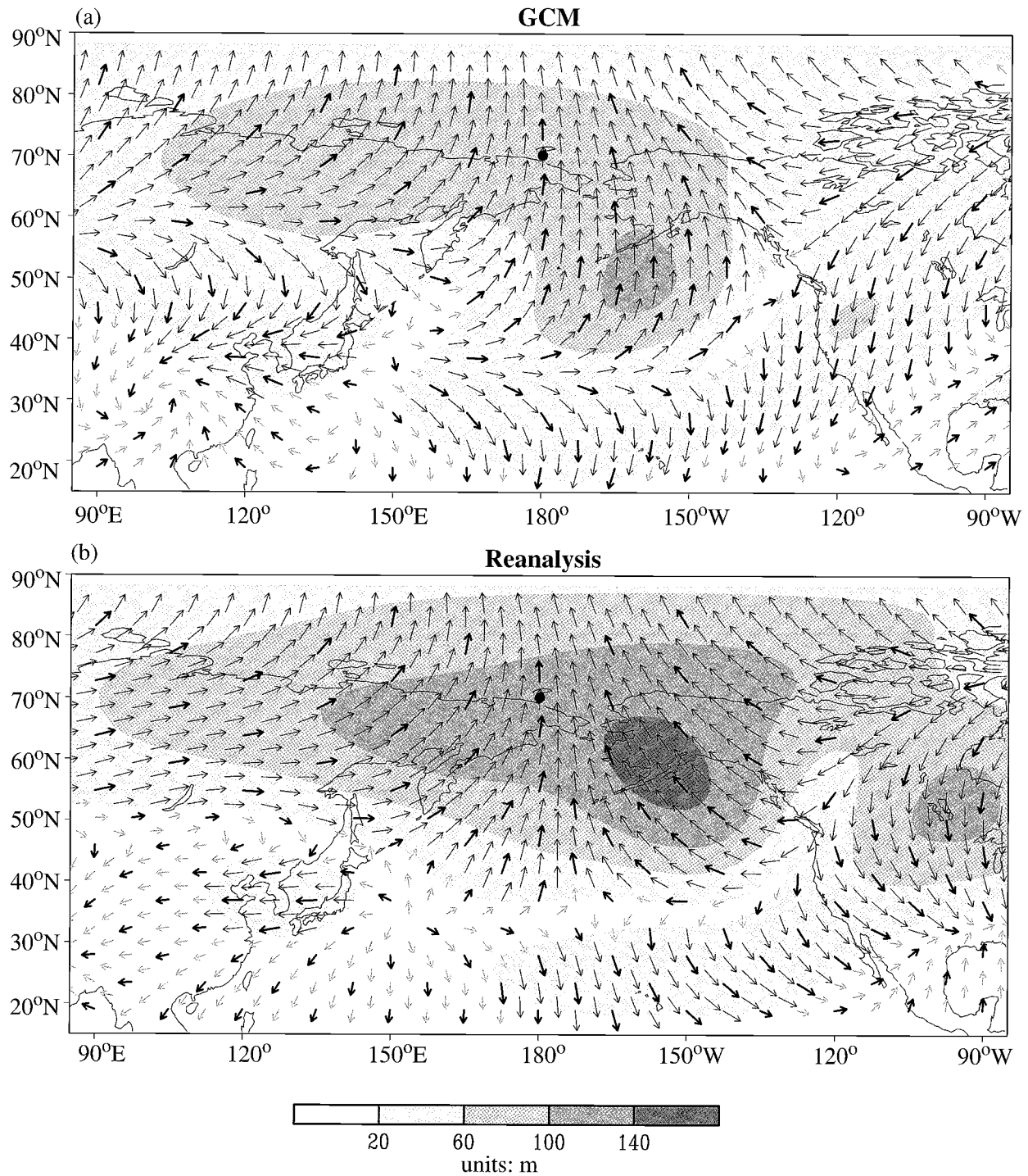
FIG. 4. Phase pattern (arrows) of the leading complex EOF of the Lanczos-filtered 300-mb height data from (a) GCM and (b) NCEP–NCAR reanalyses for the cold season. The network of 143 grid points used in the complex EOF analysis is highlighted using bolder arrows. The phase at other grid points (see thinner arrows) is obtained by temporal projection of the local 300-mb height data on the expansion coefficients of the leading complex EOF [$P_1(t)$]. The phase convention is identical to that adopted in Fig. 3: The arrow at 70°N, 180°E (indicated by a large dot) is oriented due north, and clockwise (counterclockwise) rotations indicate phase lags (leads). The amplitude of the temporal projection of 300-mb height at individual grid points on the standardized $P_1(t)$ is depicted using stippling (see scale at bottom; units: m). Short and/or gray arrows are plotted at grid points with amplitudes less than 20 m.

300 mb Z

GCM $\theta = \pi/4$ **Reanalysis**

(a)   (e)

$\theta = 2\pi/4$

(b)   (f)

$\theta = 3\pi/4$

(c)   (g)

$\theta = \pi$

(d)   (h)
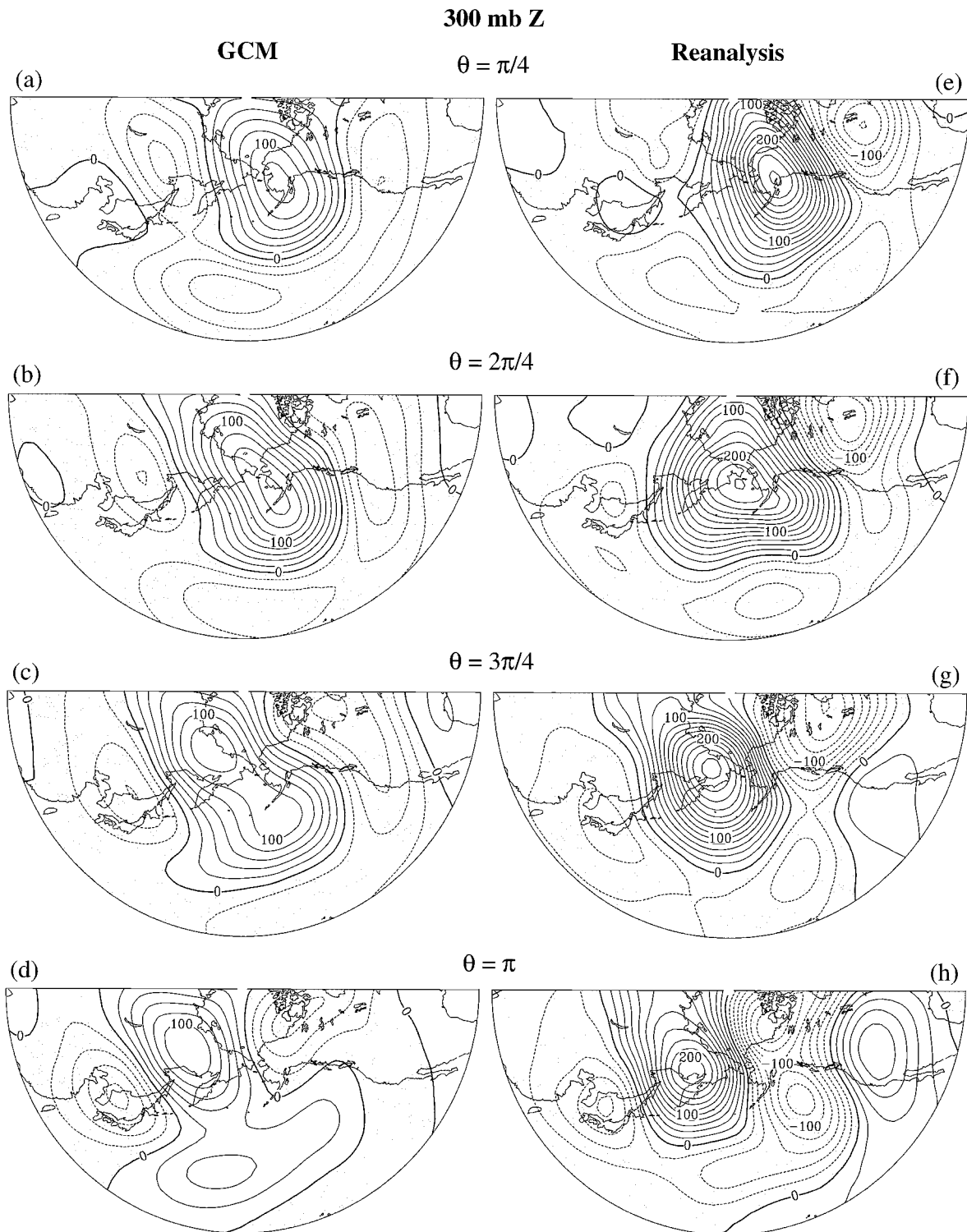
FIG. 5. Composite charts of 300-mb height anomalies for the prominent episodes as identified using the temporal coefficients of the leading complex EOF for the cold season. The patterns are based on GCM (left panels) and NCEP–NCAR (right panels) data, and correspond to temporal phases θ of [(a) and (e)] $\pi/4$, [(b) and (f)] $2\pi/4$, [(c) and (g)] $3\pi/4$, and [(d) and (h)] π. Contour interval: 20 m.

at N_p selected grid points. A Hilbert transform was performed to generate a complex time series, with the real part corresponding to the original Lanczos-filtered time series and the imaginary part being in quadrature with the real part. An $N_p \times N_p$ correlation matrix was constructed by computing the products between the complex time series at a given grid point with the corresponding series at each of the N_p points in the analysis domain. The leading principal component (i.e., that which accounts for the largest fraction of domain-integrated variance) was then obtained by eigenanalysis of this matrix. This principal component, denoted as $P_1(t)$, where t represents the time variable, is associated with a complex eigenvector pattern $e_1(s)$, where s represents the space variable. The characteristic spatial structure of the leading eigenmode may be discerned by mapping the distribution of $e_1(s)$. The temporal variations in the amplitude and phase of this mode can be deduced from the complex time series $P_1(t)$.

The above procedure has been applied to 300-mb height data in the northern cold season, for the domain extending from 90°E eastward to 90°W, and from 20° to 90°N. This longitudinal sector has been selected by virtue of the prevalent retrograde signals therein (see Fig. 3). The spatial phase patterns of the leading eigenvector $e_1(s)$ as obtained from this analysis are shown in Fig. 4 for (a) GCM and (b) reanalysis data. The number of grid points used in the complex EOF analysis (N_p) is 143. These points are chosen primarily on the basis of equal-area considerations. The locations of the N_p grid points are indicated by the bold arrows in Fig. 4. The orientation of these arrows depicts the relative phase, with a convention analogous to that used in Fig. 3. The phase arrow in the vicinity of 70°N, 180°W (i.e., the reference site RS considered in the previous section) is set to point due north in Fig. 4. The orientation of all other arrows in the domain is then determined according to the phase difference between the individual grid points and RS. Clockwise (counterclockwise) rotation of the arrows indicate phase lag (lead) relative to RS.

In order to fill in the phase information at the spatial gaps between the N_p grid points used in the eigenanalysis, as well as to estimate the typical amplitudes of the local geopotential height fluctuations associated with the leading eigenmode, the daily 300-mb height data for a grid mesh with a higher spatial resolution than the array of N_p points have been temporally projected on $P_1(t)$. The phase and amplitude information thus obtained for the finer grid is added in Fig. 4 by using thin arrows (for phase) and stippling (for amplitude). The thin arrows nicely complement the set of N_p thick arrows in providing a fuller depiction of the phase structure throughout the analysis domain. The amplitude values shown in Fig. 4 may be interpreted as the magnitude of local 300-mb height variations accompanying a change of one standard deviation in $P_1(t)$.

Both the GCM and NCEP–NCAR patterns in Fig. 4

show high-amplitude, westward-propagating signals along the 60°–80°N belt, as well as out-of-phase relationships between fluctuations in high latitudes and the subtropics over eastern Asia and the central North Pacific. The strongest fluctuations occur in the Alaska–Bering Sea sector, with typical amplitudes that are comparable to those of the maxima in rms of Lanczos-filtered data in the same region (see Figs. 1b and 1d). The eigenvector patterns in Fig. 4 also resemble those displayed in Fig. 3, confirming that the phase/coherence behavior deduced from cross-spectral analysis is associated with the leading mode of variability in the domain of interest.

The complex EOF analysis has also been performed on GCM and reanalysis data for the Northern Hemisphere in the warm season and for the Southern Hemisphere in the cold season. The leading eigenvector patterns thus obtained (not shown) are also indicative of westward-propagating, planetary-scale features in western Canada–eastern Siberia during the northern summer in both GCM and reanalysis datasets, and along the Antarctic coast facing the Indian Ocean during the southern winter in the GCM-simulated atmosphere.

We proceed to use the amplitude information in $P_1(t)$ as the basis for identifying occurrences of strong WTP. In this procedure, an "event" is defined as a string of consecutive days satisfying the following two criteria: the normalized amplitude of $P_1(t)$ must exceed 0.75 standard deviations on all days in the event, and the number of days in the string (hereafter referred to as the "duration" of that event) must be 20 or more. In any given event, the time taken for the phase of $P_1(t)$ to advance by a complete cycle of 2π, hereafter referred to as the cycle period, can be estimated using the duration (in number of days) and total phase change (in radians) from the beginning to the end of that event. For each analysis domain and season, the number of events N_e meeting the two criteria stated above have been identified in all available years. Averages of the durations and cycle periods of the N_e events were computed, and the results are shown in Table 2. In view of the sparsity of observations in the high latitudes of the Southern Hemisphere, results based on reanalysis data in that region are not presented. The fraction of variance explained by the leading eigenvectors as well as some additional statistics on the frequency of occurrence of the identified events are also provided in this table.

While interpreting the data presented in Table 2, it should be borne in mind that many of the entries are dependent on the amplitude (>0.75) and persistence (>20 days) criteria used to select the events. The specific choices made here are based on the observation that the phase of $P_1(t)$ always increases monotonically with time when the amplitude exceeds 0.75, and that the timescale for a complete cycle is ~20 days. Experimentation with other amplitude and persistence thresholds indicates that the average cycle period is not significantly affected by specific choices of these criteria.

TABLE 2. Statistics on the cycle period, duration, and frequency of occurrence of prominent retrograde events in various seasons and in the two hemispheres, as deduced from the amplitude of the temporal coefficients of the leading complex EOF $[P_1(t)]$ for 300-mb height data from the GCM and NCEP–NCAR reanalyses.

	Northern Hemisphere				Southern Hemisphere May–Sep
	Nov–Mar		May–Sep		
	GCM	Reanalysis	GCM	Reanalysis	GCM
Fraction of variance explained by $P_1(t)$ in %	16.5	16.5	10.0	9.6	23.4
Total number of identified events (N_e)	158	30	133	36	136
Average duration (day)	35.8	36.9	30.6	29.7	31.7
Average cycle period (day)	21.8	22.4	22.1	21.4	19.8
Average number of cycles in each event	1.6	1.7	1.4	1.4	1.6
Average number of events in each 5-month season	1.6	1.4	1.4	1.7	1.4
Fraction (in %) of 5-month seasons with: no event	9	18	15	19	17
1 event	35	36	37	24	37
2 events	42	36	42	52	34
3 events	13	9	4	5	9
>3 events	0	0	0	0	1

Considerable agreement exists between the GCM and NCEP–NCAR results shown in Table 2. The computations for both hemispheres and both seasons yield very similar cycle periods of 20–22 days. These estimates are almost identical to those reported by Branstator (1987) and Kushnir (1987). During the northern winter, the events typically last for ~1.5 cycles. The corresponding duration in the northern warm season is relatively shorter. In a majority of the warm or cold seasons, one to two events can be identified for each five-month period. Some of the statistics displayed in Table 2 may be compared with those compiled by Madden and Speth (1989, their Table 1) for westward-traveling disturbances with zonal wavenumber 1. Our estimates of the cycle period are noticeably longer than the ~16-day periods reported by Madden and Speth. Further diagnosis is needed to determine whether the 16-day waves and the WTP correspond to the same physical entity. It is likely that the precise timescale is somewhat dependent on the methodology being applied in various studies. Madden and Speth (1989) have noted that, by considering only those events with obvious westward propagation, their results may be more pertinent to relatively faster moving disturbances.

A complex EOF analysis has also been performed on the GCM data with a domain corresponding to the entire extratropical Northern Hemisphere. Inspection of the spatial patterns for the first several leading eigenmodes (not shown) reveals that the retrograde signals in the subpolar latitudes of the North Atlantic are considerably weaker than those in the North Pacific. We shall henceforth focus on the characteristics of the WTP in the North Pacific sector.

7. Circulation patterns

To illustrate the typical evolution of the principal circulation features in the course of the strong events identified in the previous section, composite patterns have been constructed using the following procedure: We first specified a set of eight phases θ_i, which are separated from each other by a uniform interval of $\pi/4$, that is, $\theta_1 = 0$, $\theta_2 = \pi/4$, . . . , $\theta_8 = 7\pi/4$. For each of the N_e events satisfying the amplitude (>0.75) and duration (>20 days) criteria, the time point(s) t_i at which the phase of the leading principal component $P_1(t_i)$ is equal to each θ_i were noted. For a given θ_i, the data fields of a given variable at all the corresponding time points t_i for all N_e events were averaged. The collection of eight composite patterns thus obtained depicts the representative circulation features at regular intervals of one-eighth of a cycle (or 2–3 days).

a. 300-mb height

The composite charts of the 300-mb height anomalies at $\theta = \pi/4$, $2\pi/4$, $3\pi/4$, and π for the northern cold season are presented in Fig. 5, for GCM data (left panels) and reanalysis (right panels). The patterns corresponding to $\theta = 5\pi/4$, $6\pi/4$, $7\pi/4$, and 2π (not shown) bear a strong resemblance to those occurring a half-cycle earlier, except for a sign reversal.

Both GCM and reanalysis patterns for $\theta = \pi/4$ (Figs. 5a and 5e) are indicative of the presence of a prominent positive anomaly (ridge) centered near the Alaskan peninsula. This feature is flanked at its east, west, and south by negative anomalies (troughs) with relatively weaker
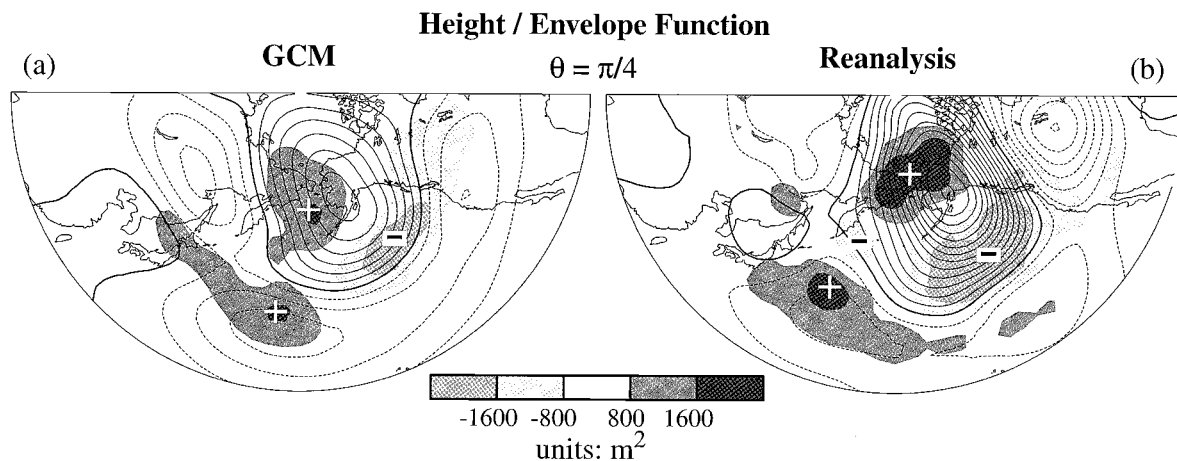
Height / Envelope Function

FIG. 6. As in Fig. 5, but for (a) GCM and (b) NCEP–NCAR composite anomalies of 300-mb height (contours, interval: 20 m) and envelope function E for synoptic-scale eddy activity (stippling, see scale bar; units: m^2) at phase $\theta = \pi/4$. Dashed contours indicate negative values. Plus and minus signs indicate centers of above- and below-normal synoptic activity, respectively.

amplitudes. The positive center is seen to move steadily westward with increasing phase, until it reaches northeastern Siberia at $\theta = \pi$ (Figs. 5d and 5h). Concurrently, the negative center over North America moves northward and then westward. The latter trough feature undergoes considerable amplification over Alaska at $\theta = 5\pi/4$ and $6\pi/4$ (not shown, but similar to the top two panels in Fig. 5 with reversed polarity) and continues on its westward journey toward the Arctic coast of Asia. Some similarities are evident between the overall development of the composite anomalies in Fig. 5 and that reported by Branstator (1987, Fig. 13) and Kushnir (1987, Fig. 11).

In the GCM pattern, the negative anomaly centered near 60°N over eastern Asia at $\theta = \pi/4$ (Fig. 5a) migrates southward as the phase advances, and the negative center over the subtropical central Pacific travels eastward from $\theta = \pi/4$ to $3\pi/4$. As the primary positive anomaly in the GCM patterns migrates westward within the 60°–70°N zone, a separate feature with the same polarity tends to remain in place over the central Pacific at 35°–45°N and persists through $\theta = 3\pi/4$ and π (see Figs. 5c and 5d). There is no evidence of the latter feature in the NCEP–NCAR reanalyses.

Comparison between the simulated and observed amplitudes shown in Fig. 5 indicates that the overall strength of the WTP is underestimated by the GCM. The relatively lower amplitudes in the GCM composites may be partially attributed to the larger number of events included therein (note from Table 2 that N_e is 158 and 30 for the GCM and reanalysis datasets, respectively).

b. Synoptic-scale activity

Over the extratropical oceans, transient disturbances with synoptic timescales of several days preferentially propagate along well-defined trajectories, or ''storm tracks'' (e.g., see Blackmon et al. 1977). Following the methodology of Nakamura and Wallace (1990), the modulation of the amplitude of storm track eddies was depicted using an envelope function E obtained as follows. A 2.5–6-day bandpass filter was first applied to the daily time series of 300-mb height. The filtered values were squared to yield the power of the high-frequency eddies and were then subjected to a 6-day lowpass filter. The function E for each grid point and each day was finally obtained by multiplying the resulting values by 2. Composite charts of the anomalies of E at temporal phase $\theta = \pi/4$ are shown using stippling in Fig. 6 for (a) GCM and (c) reanalysis data. Superposed on the stippling patterns are contours of the composite anomaly of 300-mb height at the same phase.

The patterns of E are characterized by reduction in eddy activity to the south and east of the positive 300-mb height anomaly over Alaska and by enhancement of synoptic activity to the northwest and southwest of the same anomaly. This configuration indicates that the normal west to east passage of the synoptic-scale disturbances along ~45°N is interrupted by the amplified ridge over the eastern North Pacific, with the storm track being deflected to the north and to the south on the upstream side of this ridge. The site of diminished transient activity is coincident with strong anomalous easterly flow at 300 mb. The above spatial relationships between E and the ambient circulation bear a strong resemblance to those documented by Nakamura and Wallace (1990, see their Fig. 3) for prominent blocking events in the Alaskan region.

Inspection of the composite patterns of E at the temporal phases of $\pi/2$ through 2π (not shown) indicates that the spatial relationships as noted in Fig. 6 between the anomalies in E and 300-mb height are maintained throughout the westward journey of the amplified 300-mb ridge from Alaska to eastern Siberia (see Fig. 5). The height tendency induced by anomalous eddy vorticity fluxes associated with the changes in synoptic-

scale activity has been computed using the technique described by Lau [1988, see his Eq. (1)]. The results (not shown) indicate that the perturbed eddy fluxes lead to reinforcement of the WTP-related height anomalies near the Gulf of Alaska. This positive feedback between the high-frequency transients and the more slowly varying circulation is consistent with the findings reported in Lau (1988) and Nakamura et al. (1997).

c. Sea level pressure and 850-mb temperature

The composite charts of the anomalies in sea level pressure (contours) and 850-mb temperature (stippling) at various phases are presented in Fig. 7 for the GCM (left panels) and reanalysis (right panels) data. At $\theta = \pi/4$ and $2\pi/4$, the occurrence of the enhanced 300-mb ridge over the Aleutians and the Bering Strait is coincident with an intense sea level anticyclone centered near the Gulf of Alaska (see upper four panels of Figs. 5 and 7). At the same time, the surface ridge to the east of the Rockies protrudes southward, forming a V-shaped wedge over western Canada and the central United States. This feature is particularly evident in the reanalysis patterns. The anomalous northerly flow on the eastern side of this pressure wedge brings cold Arctic air to the interior of the North American continent (see stippling in Fig. 7).[1] The negative 850-mb temperature anomaly in that region is associated with the local intensification of a pressure trough at the 300-mb level (Fig. 5). Hence the vertical structure of the pressure changes over western North America has a distinctly baroclinic character. Along the northwestern seaboard of North America, the pressure contours at $\theta = \pi/4$ and $2\pi/4$ acquire the shape of an inverted V, with vertices almost in alignment with the coastline. This pattern is accompanied by the emergence of a negative pressure anomaly center over the southwestern seaboard of North America, indicating cyclonic development along the North American coast. This coastal "troughing" is associated with rather intense sea level pressure gradients over western Canada and the Pacific Northwest. The strong anomalous easterly or southeasterly surface flows in that region bring the cold continental air masses toward the relatively warmer Pacific coasts, thus resulting in a baroclinic environment that is conducive to cyclogenesis. These coastal features are again more evident in the composites based on reanalysis data.

At $\theta = 2\pi/4$, the enhanced southerly flow on the western flank of the Alaskan anticyclone brings warm

---

[1] The temperature changes described in this and the following discussions are primarily a result of the advection of the time-averaged temperature field by the anomalous wind. The contribution due to the advection of the temperature anomalies by the time-averaged wind is weaker, since the horizontal gradient of the climatological temperature field is typically larger than that of the composite anomalous temperature pattern.

maritime air to the northeastern tip of the Asian landmass (Figs. 7b and 7f). At the same time, an extension of the positive surface pressure anomaly appears over northern Asia at 100°–120°E. The northerly flow on the eastern side of this Asian pressure wedge is accompanied by below-normal 850-mb temperatures in that region. In the GCM pattern, the enhanced horizontal temperature contrast over the northeastern coasts of Asia is seen to coincide with noticeable surface cyclonic development over the Sea of Okhotsk (Fig. 7b).

At $\theta = 3\pi/4$ and π (lower four panels in Fig. 7), the primary anticyclone crosses the Bering Sea region and arrives at northeastern Asia, in conjunction with the retrogression of the 300-mb ridge (Fig. 5). The continuity of this westward displacement in successive phases is more evident in the reanalysis data. At the same time, the cold temperature anomaly over western Canada advances toward Alaska. The surface cyclonic center over the Gulf of Alaska and the Aleutians undergoes considerable intensification. The composite patterns for the subsequent phases (not shown, but similar to those in Fig. 7 with reversed polarity) indicate that this cyclone feature eventually becomes the primary anomaly center in the sea level pressure field and migrates westward. At $\theta = 3\pi/4$ and π, the high pressure wedge in the Asian sector penetrates farther southward to eastern China. The intensified northerly flow between this wedge and the offshore cyclone leads to cold air advection in regions surrounding the east China Sea.

8. Synoptic circulation features associated with the WTP

To gain an appreciation of the flow patterns in the individual events considered in the above composite analysis, we have examined daily maps of unfiltered GCM data for several episodes with very large amplitudes of $P_1(t)$. Of particular interest is an event occurring in the January–February period in a certain year of the experiment. The averaged amplitude over the 33-day duration of this event is 1.83 standard deviations and is the highest among the $N_e = 158$ events considered in this study. The distributions of the 500-mb height, 850-mb temperature, and sea level pressure fields during two consecutive days (31 January and 1 February) in this event are shown in Fig. 8. These two days correspond to temporal phases θ of 0.39π and 0.46π, respectively.

The most prominent feature in the 500-mb height field (Figs. 8a and 8d) is the retrograding, Ω-shaped ridge over the Gulf of Alaska and Bering Sea. The height anomaly at the center of this anticyclone is as much as 600–700 m above the climatological value. A dipolelike pattern in the eastern North Pacific, with the ridge lying north of a trough, is evident in Fig. 8a. The sea level pressure field (Figs. 8c and 8f) is characterized by a strong high pressure center over Alaska and the Bering Strait, with an anomaly of 50–60 mb above normal. Comparison between Figs. 8c and 8f reveals that, within

SLP / 850 mb T

GCM Reanalysis

(a) $\theta = \pi/4$ (e)

(b) $\theta = 2\pi/4$ (f)

(c) $\theta = 3\pi/4$ (g)
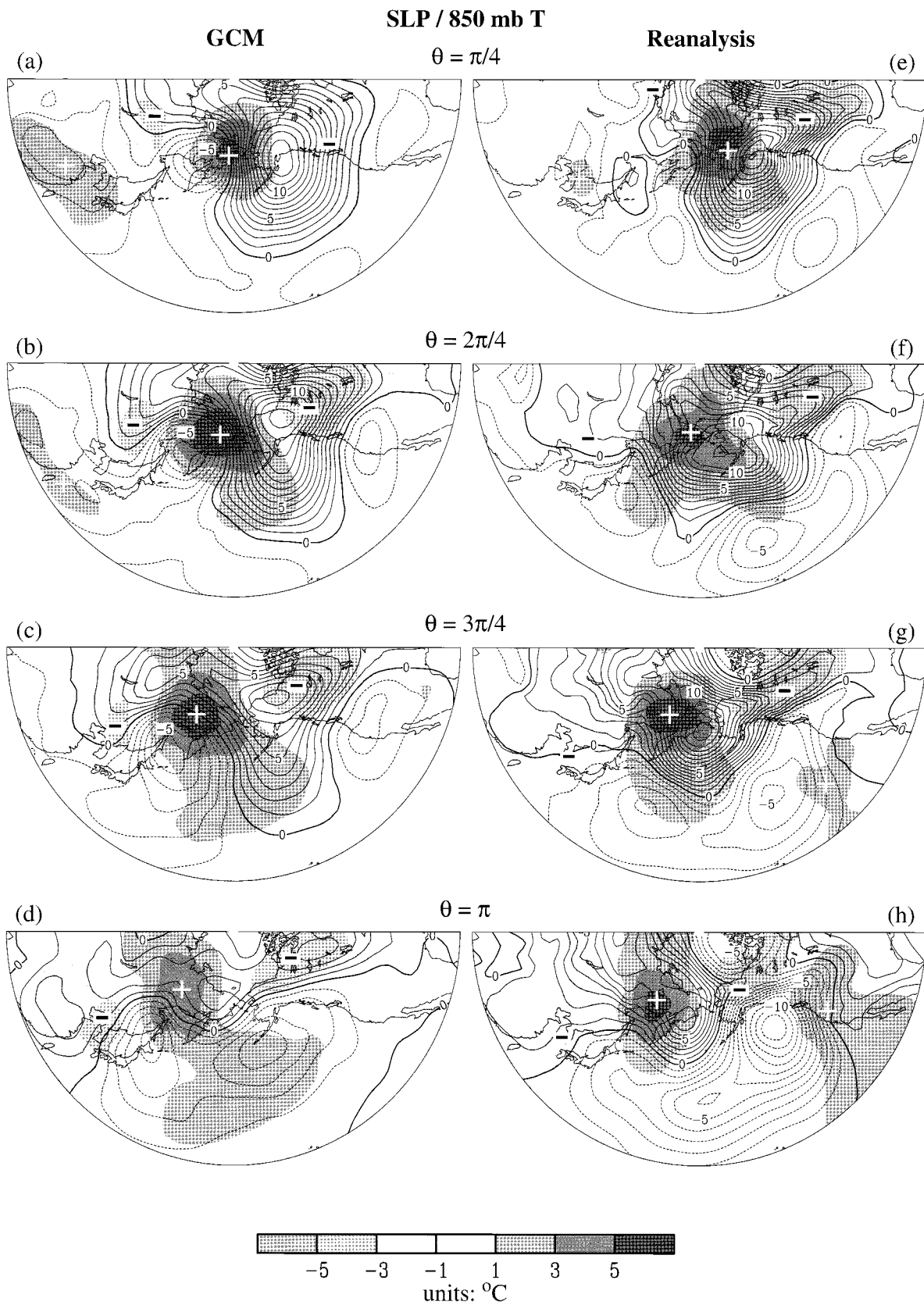
(d) $\theta = \pi$ (h)

−5 −3 −1 1 3 5

units: °C

FIG. 7. As in Fig. 5, except for sea level pressure (contours, interval: 1 mb) and 850-mb temperature (stippling, see scale bar at bottom; units: °C). Dashed contours indicate negative values. Plus and minus signs indicate warm and cold anomaly centers, respectively.
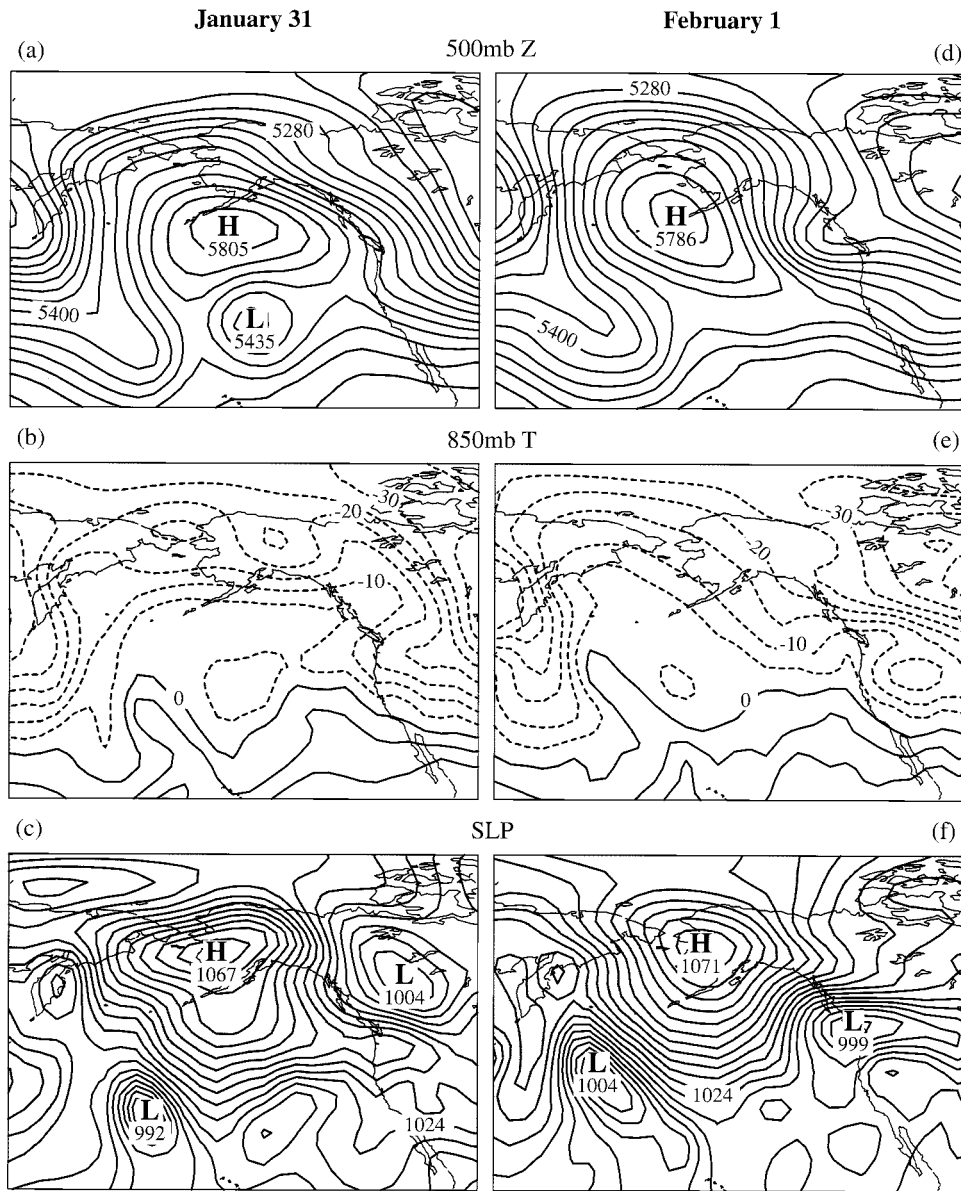
FIG. 8. Distributions of the GCM data on 31 January (left panels) and 1 February (right panels) of a selected synoptic case with a large amplitude in $P_1(t)$, for [(a), (d)] 500-mb height (contour interval: 60 m; stippling indicates values larger than 5640 m), [(b), (e)] 850-mb temperature (contour interval: 5°C; stippling indicates negative values), and [(c), (f)] sea level pressure (contour interval: 4 mb; stippling indicates values larger than 1024 mb).

the 24-h period considered here, a high pressure wedge has developed over northwestern Canada, and rapid cyclonic development has occurred over the Pacific Northwest. The one-day tendencies over the Canadian Northwest Territories and the Oregon–Washington coasts are as much as $+25$ and -35 mb, respectively. The pronounced northerly flow over western Canada and easterly flow over the Pacific coast poleward of 50°N (Figs. 8c and 8f) are seen to bring very cold Arctic air to these regions, with one-day temperature falls at 850 mb of more than 20°C over land and 10°C over the north-

eastern North Pacific (see Figs. 8b and 8e). This outbreak of cold air over the Canadian Pacific coast is accompanied by the development of a trough at 500 mb over that region (Fig. 8d), where the height drops by more than 400 m within one day. To the west of the Alaskan anticyclone, positive temperature advection by the southerly flow leads to considerable warming over western portion of the Bering Sea. Another synoptic feature of interest is the surface cyclone located near the dateline at ~35°N (Fig. 8c). This system is associated with a trough at 500 mb (Fig. 8a) and is seen to

migrate north-north-westward along the western flank of the prominent ridge.

In summary, many of the characteristics noted in the composite charts for $\theta = \pi/4$ and $2\pi/4$ (see Figs. 5–7) are discernible in the specific case study presented here. The high-amplitude signals in daily synoptic charts such as those in Fig. 8 indicate that the occurrence of WTP could have considerable impacts on local weather changes.

Ferber et al. (1993) have reported that heavy snow events in the Pacific Northwest region are coincident with a ridge near Alaska and a trough to the southeast at the upper levels, an intense surface anticyclone extending southeastward from the Gulf of Alaska to the interior of western Canada, cyclogenesis along the northwestern coast of North America, and cold 850-mb temperatures over western North America (see their Figs. 3–5). These large-scale atmospheric conditions are rather similar to those portrayed in our composite charts in Figs. 5 and 7 for $\theta = \pi/4$ and $2\pi/4$. The synoptic features noted by these authors in individual snow events (e.g., see their Fig. 7 for the case of 22 November 1985) are similar in many respects to those shown in our Fig. 8 based on GCM data. Of the four snow events occurring in Seattle after 1973 (starting year for the NCEP–NCAR dataset analyzed in the present study) and selected by Ferber et al. (1993, see their Table 1) for constructing their composites, three episodes (i.e., 8 January 1980, 22 November 1985, and 27 November 1985) are among the N_e (=30) events as identified on the basis of $P_1(t)$ described in section 6.

The equatorward protrusion of the meridionally elongated surface pressure wedge on the lee slopes of the Rockies, as well as the baroclinic structure of the local geopotential height field (i.e., negative 300-mb height anomaly overlying surface anticyclone) are reminiscent of the circulation anomalies associated with a prominent teleconnection pattern in that region, as reported in Hsu and Wallace (1985, see their Fig. 4). These authors noted that the equatorward propagation of the low-level pressure fluctuations in the vicinity of mountain ranges could partially be attributed to the equivalent beta effect associated with terrain slopes. The flow patterns presented in our Figs. 5 and 7 also exhibit some similarity with those accompanying cold surges east of the Rockies, as documented by Colle and Mass (1995, see their Figs. 2–4). The typical upper-level height pattern during these surge events, with a positive anomaly over western North America and a strong negative anomaly farther east, corresponds to an eastward displacement of the ridge–trough pattern shown in our composite for $\theta = \pi/4$ by about 40° of longitude. Among the 26 surge episodes in the post-1973 era examined by Colle and Mass (see their Table 1), 14 fall within the N_e (=30) outstanding events identified in our present study.

In the east Asian sector, the equatorward advances of the surface pressure ridge and cold Arctic air on the leeward side of the Tibetan Plateau at $\theta = 3\pi/4$ and π

(see lower four panels of Fig. 7) are similar to the synoptic development during cold air outbreaks over eastern China (e.g., see Fig. 7 of Zhang et al. 1997). These events are often accompanied by surface cyclogenesis off the Asian coast and the appearance of an upper-level pressure trough near the Sea of Japan region (e.g., see Figs. 3–4 of Lau and Lau 1984). Such circulation changes are discernible in our composite charts in Figs. 5 and 7.

Whereas the WTP may be characterized by an almost equivalent barotropic structure in the mid- and upper troposphere over the North Pacific and the surrounding low-lying land areas, the results shown in Figs. 5, 7, and 8 illustrate that the retrograde features are distinctly baroclinic in the vicinity of large-scale mountain ranges. This aspect of the WTP is less emphasized in previous studies, which are more concerned with the planetary-scale signals. For instance, the data used in the study of Branstator (1987) have been truncated to zonal wavenumber 6.

9. Vorticity tendency analysis

a. Procedure

The relative contributions of various dynamical processes to the propagation of the WTP can be diagnosed by evaluating the individual terms in the simplified vorticity tendency equation

$$\frac{\partial \zeta}{\partial t} = -v\beta - \mathbf{V} \cdot \nabla\zeta - (f + \zeta)D, \qquad (1)$$

where ζ is the relative vorticity, v the meridional wind, V the horizontal vector wind, f the Coriolis parameter, β the meridional derivative of f, and D the horizontal divergence. The three terms on the right-hand side of Eq. (1) represent the influences of planetary vorticity advection (the "β effect"), relative vorticity advection, and divergence on the time tendency of vorticity, respectively. Each of these terms was evaluated using unfiltered data for each day. Anomalies were computed by removing the climatological seasonal cycle from the daily values for these terms (see section 2 for details). The averaging procedure (as described in section 7) over the N_e identified events was then applied to these daily anomalies to compute the composite patterns for various temporal phases θ. We shall henceforth refer to the set of composite patterns thus obtained for a given term in Eq. (1) as $X(\lambda, \phi, \theta)$, where λ and ϕ denote dependences on longitude and latitude, respectively. Both the GCM and reanalysis data at 300, 500, and 850 mb for the northern cold season were analyzed in this manner. All composites were performed on the basis of the amplitude and phase of $P_1(t)$ as deduced from the height data at the 300-mb level.

It should be noted that the $-\mathbf{V} \cdot \nabla\zeta$ and ζD terms in the vorticity equation are the products of two time-varying quantities. When the above composite procedure is

used to compute these terms using unfiltered data, the results would include contributions both from the WTP fluctuations with ~three-week timescales and from storm track transients with periods of several days. As has been noted in section 7b, the latter disturbances act to reinforce the circulation patterns associated with the WTP. Hence the contributions of the high-frequency disturbances to the quadratic terms in Eq. (1) would lead to an in-phase relationship between such terms and the composite anomaly of ζ.

In order to present in a compact form the considerable amount of information in the composite results for various terms in Eq. (1), further processing of the data was performed using the following procedure.

- Averaging over latitude

The composite data were averaged over latitude from 59° to 75°N, so that we have

$$\hat{X}(\lambda, \theta) = \frac{1}{N_\phi} \sum_{\phi=59\text{N}}^{75\text{N}} X(\lambda, \phi, \theta),$$

where N_ϕ is the number of latitude rows between 59° and 75°N.

- Definition of ridge–trough categories

By applying the latitudinal averaging described above to the composite reanalysis data for Lanczos-filtered 300-mb height, and then displaying the results on the λ–θ plane, we obtain the pattern of space–time evolution of this field (see Fig. 9). Note that θ increases from top to bottom of the ordinate axis. On the basis of this diagram, a set of eight "ridge–trough categories" was determined for each longitude λ: category 3 corresponds to the maximum in height anomaly at λ (i.e., occurrence of the 300-mb ridge), category 7 to the minimum (i.e., the trough), category 1 to the crossing of the zero contour from trough to ridge, and category 5 to the zero crossing from ridge to trough. The intermediate category 2 was assigned to the midpoint (along the θ axis) between categories 1 and 3. Similarly, categories 4, 6, and 8 denote the midpoints between the category pairs (3, 5), (5, 7), and (7, 1), respectively. For each category, a line segment has been constructed by connecting the temporal phases at which that category occurs at individual longitudes. The line segments for the eight ridge–trough categories are shown in Fig. 9 using stippled curves. For instance, the line segments for categories 3 and 7 coincide with the axes of maximum and minimum anomaly in 300-mb height. We shall henceforth denote the longitude dependence of θ for the category I as $\theta_I(\lambda)$. A similar but separate categorization procedure has been performed on the basis of the pattern for the GCM height anomaly data on the λ–θ plane (not shown).

- Averaging over longitude for individual categories

For each ridge–trough category I, the latitudinal means of individual terms in Eq. (1) were then av-
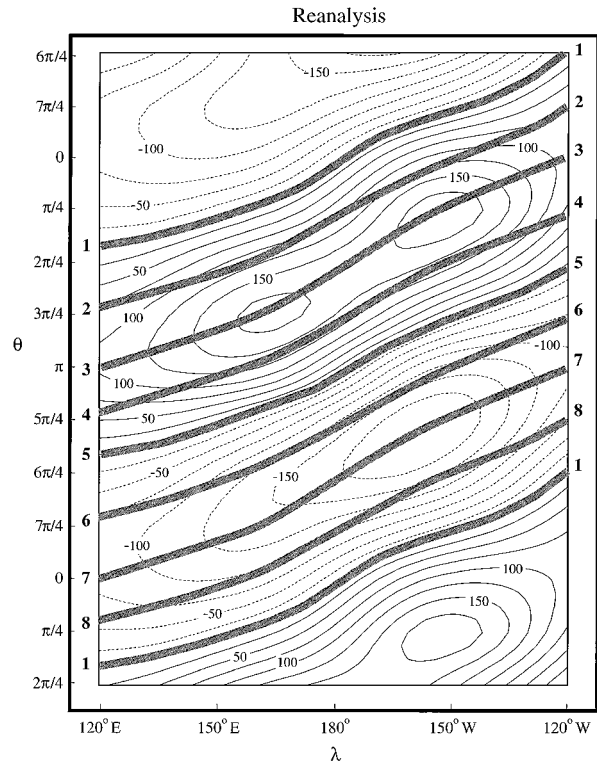

FIG. 9. Composite values of Lanczos-filtered 300-mb height anomalies for the prominent episodes identified in the NCEP–NCAR dataset using the leading complex EOF for the cold season. The results are obtained by averaging over the 59°–75°N zone and are plotted as a function of longitude and temporal phase θ. Note that θ increases from top to bottom of the ordinate axis. Contour interval: 25 m. The individual stippled line segments depict the longitudinal dependence of θ for various ridge–trough categories from 1 through 8. For each category, values of various terms in the vorticity equation have been averaged along the line segment corresponding to that category to yield the results in Fig. 10.

eraged along the stippled line segment for I on the λ–θ plane (see Fig. 9), so that we have

$$[\hat{X}]_I = \frac{1}{N_\lambda} \sum_{\lambda=120\text{E}}^{120\text{W}} \hat{X}(\lambda, \theta).$$

Here N_λ is the number of grid points in the zonal direction between 120°E and 120°W, and θ in the parentheses is a function of λ as indicated by the line segment for category I in Fig. 9, that is, $\theta = \theta_I(\lambda)$. This step hence entails the averaging of the composite data over the longitudinal span from 120°E to 120°W for each I, with the temporal phase at each longitude being determined from the ridge–trough categorization procedure described above. The set of eight values $[\hat{X}]_I$ thus obtained for each term in Eq. (1) depict the typical variations of that term relative to the ridge–trough structure of the composite wave.

b. Results

The values of the β, relative vorticity advection, and divergence terms at individual categories are displayed
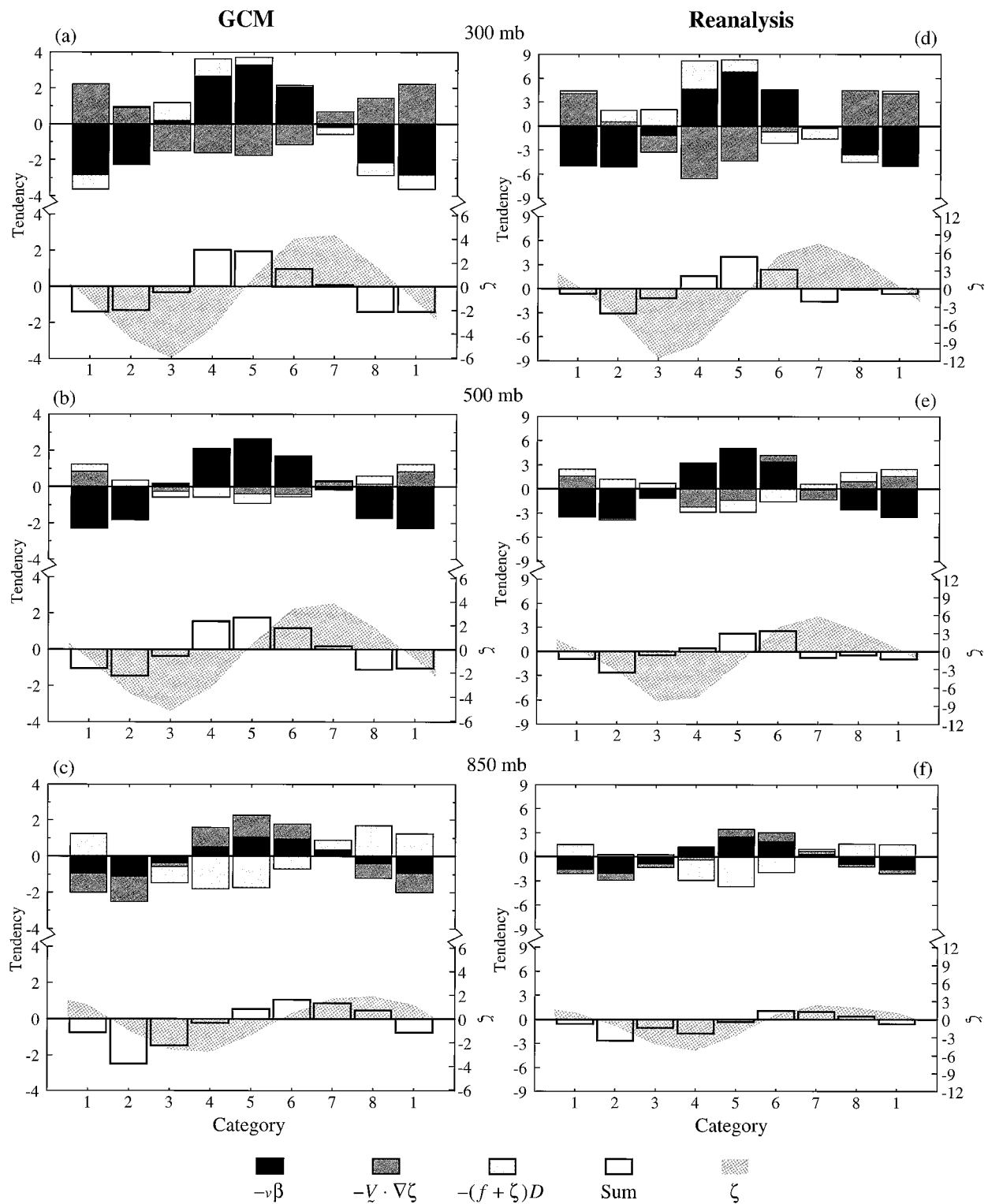
Fig. 10. Composite anomalies of individual terms in the vorticity tendency equation for various ridge–trough categories, as computed using GCM (left panels) and NCEP–NCAR (right panels) data at [(a), (d)] 300, [(b), (e)] 500, and [(c), (f)] 850 mb. See text for details of the composite procedure. In the upper portion of each panel, the β, relative vorticity advection, and divergence terms are displayed in a cumulative fashion. The sum of the three terms (bar graphs) and the composite relative vorticity (stippling) are shown in the lower panel. The scale for various terms in the vorticity tendency equation is indicated along the left ordinate axis (units: 10^{-11} s^{-2}). The scale for vorticity is indicated along the right ordinate axis in the lower part of each panel (units: 10^{-6} s^{-1}).

TABLE 3. Climatological values of the zonal wind speed (in m s^{-1}) at individual tropospheric levels during the cold season, as obtained by averaging the GCM and NCEP–NCAR reanalysis data over the region of 59°–75°N, 120°E–120°W.

	GCM	Reanalysis
300 mb	3.3	6.1
500 mb	1.5	3.1
850 mb	−1.5	−0.7

in a cumulative format in Fig. 10 for GCM data (left panels) and reanalysis (right panels) at 300 (top), 500 (middle), and 850 mb (bottom). Also shown in the lower half of the same panels are the sum of the three terms (bar graphs) and the relative vorticity (stippling).

The following considerations are helpful for interpreting the results presented in Fig. 10. In accord with the westward propagation of the composite wave, the principal features in the contour pattern in Fig. 9 exhibit a distinct tilt toward increasing temporal phase as they are scanned from east to west. The line segments for each of the ridge–trough categories are also characterized by a similar tilt. It is evident from the configuration of these line segments that, if the category I_o occurs at longitude λ_o and temporal phase θ_o, then the categories $I_o - 1$, $I_o - 2$, etc., would occur to the *west* of λ_o at the same θ_o. Conversely, categories $I_o + 1$, $I_o + 2$, etc., would occur to the *east* of λ_o at θ_o. In other words, the abscissa of the panels in Fig. 10 may alternatively be viewed as the longitudinal axis for a fixed temporal phase, so that the data shown in these panels describe the changes from west to east at a given time as the ridge–trough category progresses from 1 to 8. In the following discussion, we shall make use of this equivalence between wave category and longitudinal displacement, and shall refer to the results in Fig. 10 mostly in terms of east–west variations through a complete wavelength of the composite WTP.

For both the simulated and observed atmospheres, the vorticity budget at 500 mb (Figs. 10b and 10e) is dominated by the β term. The $(f + \zeta)D$ term is small due to the weak horizontal divergence at this level. The advection of the relative vorticity anomaly by the zonal flow (which is a main contributor to the $-\mathbf{V} \cdot \nabla\zeta$ term) is also weak due to the much diminished mean circulation in the Alaska–eastern Siberia sector (see Figs. 1a and 1c and Table 3). The sum of the three terms in the vorticity equation (see bar graphs in lower part of Figs. 10b and 10e) is hence similar to the β term. The quadrature relationship between the total vorticity tendency and the relative vorticity curve (see stippling) leads to westward propagation of the composite wave. This relationship is primarily the result of positive (negative) planetary vorticity advection at a quarter-wavelength to the west of the trough (ridge).

At the 300-mb level (Figs. 10a and 10d), both the relative vorticity advection and divergence terms are stronger than those at 500 mb. Advection of the vorticity

anomalies by the prevalent westerly flow (see Table 3) opposes the β effect, with the β term being relatively larger. The divergence term tends to have the same polarity as the β term in most ridge–trough categories. The phasing of the net tendency due to all three terms relative to the relative vorticity curve is still conducive to westward propagation (see lower part of Figs. 10a and 10d).

At the 850-mb level (see Figs. 10c and 10f), the easterly ambient zonal flow poleward of the Aleutian low (see Table 3 in this paper and Fig. 43 of Alexander and Scott 1995) accounts for the westward tendency associated with relative vorticity advection. The combined effects of planetary and relative vorticity advection are seen to be partially offset by the divergence term. The net tendency (lower bar graphs of Figs. 10c and 10f) results again in westward propagation.

The apparent lack of an in-phase relationship between the $-\mathbf{V} \cdot \nabla\zeta$ term and the composite anomaly of ζ at all three levels suggests that the positive feedback effects between the WTP and high-frequency transients (see discussion in sections 7b and 9a) do not contribute significantly to the vorticity tendency when averages are taken over the broad domain between 120°E and 120°W. However, there could still be strong dynamical interactions between the storm track eddies and the slowly varying ambient circulation in more localized sites such as the Gulf of Alaska (see Nakamura et al. 1997).

10. Interpretations

a. Vorticity equation

It is possible to gain some physical insight in the phase relationships among the various terms as shown in Fig. 10 by examining the linearized and quasigeostrophic version of Eq. (1), for example, see Holton [1992, Eq. (7.89)],

$$\frac{\partial}{\partial t}\nabla^2\psi = -\frac{\partial\psi}{\partial x}\beta - \overline{u}\frac{\partial}{\partial x}\nabla^2\psi - fD, \qquad (2)$$

where ψ is the perturbation streamfunction, x the distance in the zonal direction, and $\overline{u}$ the basic state zonal wind, which is a function of height only. The vorticity of the basic state is assumed to be small compared with f. We consider a wavelike solution with a phase speed c that is invariant with height, that is, $\psi = \tilde{\psi}e^{ik(x-ct)}$, and an analogous form for the divergence $D = \tilde{D}e^{ik(x-ct)}$. Here k is the zonal wavenumber, the tilde denotes the complex amplitude, and latitudinal dependence is ignored. At the nondivergent level (which is close to the 500-mb surface; see Fig. 10), where $D = 0$, we then obtain the familiar Rossby wave formula $c = \overline{u}_o - \beta/k^2$. Here $\overline{u}_o$ denotes the basic state zonal wind at the nondivergent level. At an arbitrary altitude, it can be shown from Eq. (2) that $\tilde{D} = (ik^3/f)(\overline{u} - \overline{u}_o)\tilde{\psi}$. This result indicates that at those altitudes where $\overline{u} > \overline{u}_o$ (as in the case of 300 mb; see Table 3), the maximum divergence

occurs at a quarter-wavelength to the east of the maximum vorticity. Conversely, at levels where $\overline{u} < \overline{u}_o$ (e.g., 850 mb; see Table 3), the divergence center is situated at a quarter-wavelength to the west of the vorticity center. The evidence presented in Fig. 10 is in accord with these phase relationships.

The above analysis delineates the role of the divergence term in maintaining a constant phase speed c for the entire tropospheric column. In the upper troposphere, the stronger westerlies (as compared to $\overline{u}_o$) advect the eddy vorticity eastward and hence act to oppose the β effect. In order for the upper-level wave to have the same phase speed as that for the nondivergent level, the divergence pattern in the upper troposphere must offset the advection of ζ by $\overline{u}$; that is, divergence (which leads to negative vorticity tendency) must be situated to the east of the maximum ζ. By the same token, the easterly basic state in the lower troposphere acts in concert with the β effect by advecting ζ westward. The excessive westward tendency (as compared with that at the nondivergent level) that results is offset by the presence of divergence to the west of maximum ζ.

b. Temperature equation

The processes contributing to the evolution of the temperature perturbations T near 500 mb may be discerned from the linearized quasigeostropic thermodynamic equation, for example, see Holton [1992, Eq. (3.6)],

$$\frac{\partial T}{\partial t} = -v\frac{\partial}{\partial y}\overline{T} - \overline{u}\frac{\partial T}{\partial x} + S_p\omega, \qquad (3)$$

where v is the perturbation meridional velocity, $\partial\overline{T}/\partial y$ the meridional gradient of the basic state temperature, S_p the static stability parameter, and ω the perturbation vertical velocity in pressure coordinates. We assume that, away from regions of high terrain, the retrograde perturbations in geopotential height have an almost equivalent barotropic structure in the mid- and upper troposphere, and that their amplitude increases with height (as is evident from the composite data of ζ presented in Fig. 10). Hence pressure ridges (troughs) are collocated with warm (cold) midtropospheric temperatures near the 500-mb level. For a basic state with $\partial\overline{u}/\partial p < 0$ and $\partial\overline{T}/\partial y < 0$, the first term on the rhs of Eq. (3) leads to negative temperature tendency west of the cold trough and warm temperature tendency west of the warm ridge, thus causing the temperature perturbation at $\sim$500 mb to migrate westward. For a midtropospheric basic state with $\overline{u} > 0$, the second term in Eq. (3) results in eastward displacement of the perturbations in T. Recalling the phase relationships between the horizontal divergence D and the troughs and ridges at various altitudes [see Fig. 10 and the above analysis of Eq. (2)], and invoking mass continuity, it is seen that the midtropospheric vertical motion is directed upward east of the trough and downward east of the ridge. The resulting adiabatic cooling and warming [third term in Eq. (3)] lead to eastward propagation of T. In summary, the net temperature tendency is determined by the balance between competing effects of $-v\partial\overline{T}/\partial y$ on the one hand and $-\overline{u}\partial\overline{T}/\partial x + S_p\omega$ on the other. The salient westward migration of T in Fig. 7 signifies that $-v\partial\overline{T}/\partial y$ is the dominant term in Eq. (3).

11. Discussion

The results presented in this study confirm the findings by Branstator (1987) and Kushnir (1987) that the WTP constitute a significant mode of variability of the tropospheric circulation in high latitudes on intraseasonal timescales. As further evidence of the critical role of the WTP in atmospheric variability on these timescales, we have computed the seasonal average of the amplitude of the temporal coefficients for the leading complex EOF [i.e., $P_1(t)$] for individual winters and contrasted the winters with mean amplitudes within the top 20th percentile with those in the bottom 20th percentile. The results (not shown) indicate that the rms of Lanczos-filtered 300-mb height over the Bering Sea region in the former group of winters exceed the same quantity in the latter group by $\sim$30 and 45 m in the model and observed atmospheres, respectively. These differences correspond to approximately one-third of the mean rms amplitude for all winters (see Figs. 1b and 1d). Hence the presence or absence of WTP activity is a major determining factor of the level of low-frequency variability in individual seasons. It is also noteworthy that the composite of seasonally averaged 300-mb height anomaly for the group of winters with active WTP (not shown) is characterized by a well-defined pattern in the Pacific–North American sector. The polarity of this pattern in reversed in the composite for the winters in the bottom 20th percentile. Further study is required to delineate the linkages between the level of WTP activity and the structure of the seasonally averaged basic state.

Diagnosis of the vorticity tendency equation reveals that the behavior of the WTP is in essence governed by Rossby wave dynamics. In regions where the mean zonal flow is weak (such as the Alaska–Siberia sector), the dominance of the β effect leads to westward propagation. In view of the notable geographical dependence of the time mean flow, analysis tools that focus on local characteristics may be better suited for studying the nature of the WTP phenomena, as opposed to many of the earlier works that describe the retrograde features using global basis functions such as zonal or spherical harmonics.

The circulation charts presented in sections 7 and 8 illustrate that the occurrence of WTP in certain geographical regions is accompanied by synoptic features that exert strong influences on the local weather. Of particular interest are the link between specific phases of the WTP with the incidence of cold air surges on the

lee slopes of the Rockies and snowstorms along the northwestern coasts of North America, and the reorientation of the Pacific stormtrack during prominent episodes of the WTP. The regularity and periodicity of space–time evolution of the low-frequency retrograde phenomena could perhaps be exploited in the development of forecast schemes for these weather events.

Few investigations have thus far been performed on the simulation of WTP in GCMs. [Prior to the present work, Kushnir (1987) has examined this phenomenon in a two-level, $4° × 5°$ GCM developed at Oregon State University.] In conducting our study, we have made a systematic effort to analyze the GFDL GCM and NCEP–NCAR datasets using the same set of procedures, and we have compared in detail the model and observational results thus obtained. It is demonstrated that the GCM is capable of reproducing many facets of the observed WTP, including three-dimensional structure, timescale, preferred site of activity, vorticity dynamics, and interaction with synoptic-scale disturbances. The good performance of the GCM in simulating this low-frequency phenomenon lends credence to its usefulness for studying extratropical atmospheric variability on intraseasonal timescales.

The GCM tool offers several unique advantages for investigating various aspects of the WTP. The controlled environment in the model atmosphere allows for the study of the behavior of WTP in various basic states and external conditions. The model output provides an alternative data source for estimating those quantities that are difficult to evaluate based on observations only (such as horizontal divergence in the vorticity tendency equation). Extended GCM integrations also generate time series that far exceed in length those based on the available observational records, so that the phenomena of interest can be sampled more adequately using the GCM datasets.

As an illustration of the potential applications of the GCM tool for enhancing our knowledge of the WTP, it is noteworthy that we have detected these retrograde features in a model run with no interannual variability in the boundary conditions. The implication of this model result is that such fluctuations are mostly generated by internal atmospheric processes. It remains to ascertain the extent to which the location, intensity, and frequency of occurrence of these WTP may be affected by perturbed boundary forcings, either through modification of the stationary background flow or through generation of teleconnection patterns that have strong spatial projection on certain phases of the WTP. These outstanding issues could be addressed by diagnosing the output from model simulations subjected to anomalies in the boundary conditions. For instance, the impact of sea surface temperature (SST) changes in various parts of the World Ocean on the behavior of the WTP could be assessed using the suite of SST sensitivity experiments similar to those described by Lau and Nath (1994).

Recently, increased use of the ensemble approach has been made in numerical prediction and in model studies of the atmospheric responses to external forcing. An important issue in the application of this approach is the nature of the scatter among individual members of a given ensemble. Examples of such intersample variability have been presented by Tracton and Kalnay (1993) in a forecasting context, and by Lau and Nath (1994) for an SST sensitivity study. In view of the large amplitude and long period of the WTP, the differences between multiple realizations in an ensemble could partially be attributed to differences in the level of activity of these retrograde disturbances. Hence much could be gained by applying our knowledge of the characteristics of WTP to the interpretation of the model products generated by ensemble forecasts on seasonal timescales or by multiple runs subjected to an identical forcing scenario.

REFERENCES

Ahlquist, J., 1982: Normal-mode global Rossby waves: Theory and observations. *J. Atmos. Sci.,* **39,** 193–202.

Alexander, M. A., and J. D. Scott, 1995: Atlas of climatology and variability in the GFDL R30S14 GCM. Tech. Report. [Available from CDC/NOAA, R/E/CD1, 325 Broadway, Boulder, CO 80303-3328.]

Anderson, J. L., 1991: The robustness of barotropic unstable modes in a zonally varying atmosphere. *J. Atmos. Sci.,* **48,** 2393–2410.

Arai, Y., 1970: A statistical study of ultra-long waves. *J. Meteor. Soc. Japan.,* **48,** 469–478.

Blackmon, M. L., J. M. Wallace, N.-C. Lau, and S. L. Mullen, 1977: An observational study of the Northern Hemisphere wintertime circulation. *J. Atmos. Sci.,* **34,** 1040–1053.

Branstator, G., 1987: A striking example of the atmosphere's leading traveling pattern. *J. Atmos. Sci.,* **44,** 2310–2323.

——, and I. Held, 1995: Westward propagating normal modes in the

presence of stationary background waves. *J. Atmos. Sci.,* **52,** 247–262.

Broccoli, A. J., and S. Manabe, 1992: The effects of orography on midlatitude Northern Hemisphere dry climates. *J. Climate,* **5,** 1181–1201.

Colle, B. A., and C. F. Mass, 1995: The structure and evolution of cold surges east of the Rocky Mountains. *Mon. Wea. Rev.,* **123,** 2577–2610.

Deland, R. J., 1964: Traveling planetary waves. *Tellus,* **16,** 271–273.

——, 1965: Some observations of the behavior of spherical harmonic waves. *Mon. Wea. Rev.,* **93,** 307–312.

Duchon, C., 1979: Lanczos filtering in one and two dimensions. *J. Appl. Meteor.,* **18,** 1016–1022.

Eliasen, E., and B. Machenhauer, 1965: A study of the fluctuations of atmospheric planetary flow patterns represented by spherical harmonics. *Tellus,* **17,** 220–238.

Ferber, G. K., C. F. Mass, G. M. Lackmann, and M. W. Patnoe, 1993: Snowstorms over the Puget Sound lowlands. *Wea. Forecasting,* **8,** 481–504.

Haurwitz, B., 1940a: The motion of atmospheric disturbances. *J. Mar. Res.,* **3,** 35–50.

——, 1940b: The motion of atmospheric disturbances on the spherical earth. *J. Mar. Res.,* **3,** 254–267.

Hayashi, Y., 1971: A generalized method of resolving disturbances into progressive and retrogressive waves by space Fourier and time cross-spectral analyses. *J. Meteor. Soc. Japan,* **49,** 125–128.

Holton, J. R., 1992: *An Introduction to Dynamic Meteorology.* 3d ed. Academic Press, 511 pp.

Horel, J., 1984: Complex principal component analysis: Theory and examples. *J. Climate Appl. Meteor.,* **23,** 1660–1673.

Hough, S. S., 1898: On the application of harmonic analysis to the dynamical theory of tides, II, On the general integration of Laplace's dynamical equations. *Philos. Trans. Roy. Soc. London, Series A,* **191,** 139–185.

Hsu, H.-H., and J. M. Wallace, 1985: Vertical structure of wintertime teleconnection patterns. *J. Atmos. Sci.,* **42,** 1693–1710.

Huang, H.-P., and W. A. Robinson, 1995: Barotropic model simulations of the North Pacific retrograde disturbances. *J. Atmos. Sci.,* **52,** 1630–1641.

Julian, P. J., 1975: Comments on the determination of significance levels of the coherence statistic. *J. Atmos. Sci.,* **32,** 836–837.

Kalnay, E., and Coauthors, 1996: The NCEP/NCAR 40-year Reanalysis Project. *Bull. Amer. Meteor. Soc.,* **77,** 437–471.

Kushnir, Y., 1987: Retrograding wintertime low-frequency disturbances over the North Pacific Ocean. *J. Atmos. Sci.,* **44,** 2727–2742.

Lanzante, J. R., 1990: The leading modes of 10–30-day variability in the extratropics of the Northern Hemisphere during the cold season. *J. Atmos. Sci.,* **47,** 2115–2140.

Lau, N.-C., 1988: Variability of the observed midlatitude storm tracks in relation to low-frequency changes in the circulation pattern. *J. Atmos. Sci.,* **45,** 2718–2743.

——, and K.-M. Lau, 1984: The structure and energetics of midlatitude disturbances accompanying cold-air outbreaks over East Asia. *Mon. Wea. Rev.,* **112,** 1309–1327.

——, and M. J. Nath, 1987: Frequency dependence of the structure and temporal development of wintertime tropospheric fluctuations—Comparison of a GCM simulation with observations. *Mon. Wea. Rev.,* **115,** 251–271.

——, and ——, 1994: A modeling study of the relative roles of tropical and extratropical SST anomalies in the variability of the global atmosphere–ocean system. *J. Climate,* **7,** 1184–1207.

Lejenäs, H., and R. A. Madden, 1992: Traveling planetary-scale waves and blocking. *Mon. Wea. Rev.,* **120,** 2821–2830.

Lindzen, R. S., D. M. Straus, and B. Katz, 1984: An observational study of large-scale atmospheric Rossby waves during FGGE. *J. Atmos. Sci.,* **41,** 1320–1335.

Madden, R. A., 1978: Further evidence of traveling planetary waves. *J. Atmos. Sci.,* **35,** 1605–1618.

——, 1979: Observations of large-scale traveling Rossby waves. *Rev. Geophys. Space Phys.,* **17,** 1935–1949.

——, and P. R. Julian, 1972: Further evidence of global-scale 5-day pressure waves. *J. Atmos. Sci.,* **29,** 1464–1469.

——, and P. Speth, 1989: The average behavior of large-scale westward traveling disturbances evident in the Northern Hemisphere geopotential heights. *J. Atmos. Sci.,* **46,** 3225–3239.

Nakamura, H., and J. M. Wallace, 1990: Observed changes in baroclinic wave activity during the life cycles of low-frequency circulation anomalies. *J. Atmos. Sci.,* **47,** 1100–1116.

——, M. Nakamura, and J. L. Anderson, 1997: The role of high- and low-frequency dynamics in blocking formation. *Mon. Wea. Rev.,* **125,** 2074–2093.

Panofsky, H. A., and G. W. Brier, 1958: *Some Applications of Statistics to Meteorology.* Pennsylvania State University, 224 pp.

Platzman, G. W., 1968: The Rossby wave. *Quart. J. Roy. Meteor. Soc.,* **94,** 225–248.

Rossby, C.-G., and Coauthors, 1939: Relations between variations in the intensity of the zonal circulation of the atmosphere and the displacements of the semipermanent centers of action. *J. Mar. Res.,* **2,** 38–55.

Salby, M. L., 1984: Survey of planetary-scale traveling waves: The state of theory and observations. *Rev. Geophys. Space Phys.,* **22,** 209–236.

Tracton, M. S., and E. Kalnay, 1993: Operational ensemble prediction at the National Meteorological Center: Practical aspects. *Wea. Forecasting,* **8,** 379–398.

Zhang, Y., K. R. Sperber, and J. S. Boyle, 1997: Climatology and interannual variation of the east Asian winter monsoon: Results from the 1979–95 NCEP–NCAR reanalysis. *Mon. Wea. Rev.,* **125,** 2605–2619.